Deformation characteristics and formability of a tricot-stitched carbon fiber unidirectional non-crimp fabric

Mehdi Ghazimoradi[1], Eleazar A. Trejo[1], Valter Carvelli[2], Clifford Butcher[1], John Montesano[1]*

[1] Department of Mechanical & Mechatronics Engineering, University of Waterloo, 200 University Ave. West, Waterloo N2L 3G1, Canada

[2] Department A.B.C., Politecnico di Milano, Piazza Leonardo Da Vinci 32, 20133 Milan, Italy

* Corresponding Author: john.montesano@uwaterloo.ca

Abstract

Deformation characteristics and formability of a heavy-tow unidirectional non-crimp fabric (UD-NCF) was studied. The fabric response under in-plane shear and biaxial tension loading (experienced during forming operations) was first investigated. Local deformations captured by measuring tensile/compressive strains in the stitching segments traversing the carbon fiber tows was correlated to the fabric three-stage macroscopic response during shear tests. Biaxial tension tests were performed at room and elevated temperatures with different displacement ratios to mimic typical preforming processes. Variations in biaxial displacement ratio revealed the interdependency of the fabric orthogonal tensile deformation modes, while temperature did not influence the response. Next, single layer hemispherical and flat punch draping experiments were performed to monitor defects (wrinkling) and capture strain contours, which correlated with in-plane shear and biaxial tension deformations. The results yield an improved understanding of the complex multiscale deformation modes for the heavy-tow UD-NCF and represent important data sets for constitutive models.

Keywords: A: non-crimp fabric (NCF); B: mechanical properties; D: microstructural analysis; E: preforming.

Journal Pre-proofs

1. Introduction

High pressure resin transfer molding (HP-RTM) has recently emerged in the automotive industry as a robust and rapid process to produce small and medium sized carbon fiber reinforced plastic (CFRP) composite components, with the potential for use in high-volume production applications [1]. Rapid production rates are achieved in part by automating the HP-RTM process steps, including preforming of the fabric layers prior to infusing with the liquid resin. Preforming of the fabric layers involves draping within the mold itself or more commonly using a separate draping tool [2,3]. One of the challenges with preforming is that defects, such as wrinkling and excessive shear deformations, can be introduced into the dry fabric layers, leading to flaws and local weakening of the composite components. Therefore, simulation of the draping process can be utilized to predict these defects and to optimize the fabrication process [4,5]. To this end, characterization of the corresponding fabric response under the deformation modes experienced during preforming becomes essential to calibrate any draping simulation model.

In recent years, stitched unidirectional non-crimp fabrics (UD-NCFs) have been widely used for manufacturing low cost composite parts in various industry sectors, including the automotive industry [6]. Owing to their formability and permeability characteristics, UD-NCFs are suited for an HP-RTM process [7–9]. Unlike several woven fabrics, which consist of two sets of interlacing yarns (i.e., warp and weft), the aligned tows in UD-NCFs are bound together with a light stitching yarn and are often supported by transverse fiber yarns. The type of stitching yarn and the stitching architecture directly influence the local fabric deformation and the in-plane/out-of-plane macroscopic deformation modes, which significantly affects the draping behavior of UD-NCFs [10]. In the studies by Krieger et al. [10] and Lomov [11], the stitching angle with respect to the tow, stitching pitch, stitching yarn thickness variation and the stitching loop structure notably influenced the formability of UD-NCFs. One of the challenges with UD-NCFs is that they are generally susceptible to high degree of local distortions and tow gapping during forming processes, which can be detrimental to the performance of the corresponding CFRP part [12]. In the study by Krieger et al. [13], tailored NCFs were designed for components by defining unique stitching parameters in different local regions to minimize defects in highly deformed zones. However, tailoring the stitching pattern and architecture is not always feasible in cases where pre-stitched UD-NCF are required to fabricate cost-effective CFRP parts. Therefore, it is important to evaluate the factors affecting the mechanical behavior of UD-NCFs under various deformation modes experienced during a forming process.

In-plane shear deformation is one of the main deformation modes experienced by fabrics during forming. To characterize the in-plane shear properties of fabric reinforcements, the 45° off-axis extension (or bias extension) and picture frame tests have been widely utilized [14,15]. Few experimental studies have been dedicated to investigating the shear behavior of UD-NCFs (see e.g. [9,15–18]). Pourtier et al. [17] studied the distribution of shear angle in NCFs during off-axis extension tests. It was revealed that deformed specimens had three distinct deformation zones, where a simple shear approximation was deemed most accurate. A similar shear deformation response was observed by Trejo et al. [16] for UD-NCF off-axis extension specimens. Schirmaier et al. [4] reported the results of a comprehensive study on in-plane shear deformation mechanism of a UD-NCF, and recommended the use of a 45^0 off-axis extension test to more accurately capture the shear deformation response. Furthermore, picture frame tests have been extensively adopted for shear characterization of woven textiles [19–24], while only being considered by few groups for UD-NCFs [7].

In addition to in-plane shear deformation, the response of fabrics under in-plane biaxial tension loading also plays an important role during the forming processes [23, 24]. For woven fabrics, the interaction between warp and weft yarns directly influences the biaxial tension response of the fabric [26]. In UD-NCFs, the interaction between longitudinal tows and transverse supporting yarns are completely different due to the stitching and the fact that tows and yarns are not interlaced. There have been few studies focused on characterizing the biaxial tension response of UD-NCFs and highlighting the importance of this deformation mode for fabric draping (see e.g. [24, 26]).

Typical fabric forming processes are performed at elevated temperatures to activate the binder and hold the formed fabric layers into the desired shape for subsequent liquid resin infusion. Thus, the performance of fabric reinforcements at elevated temperatures is important since temperature may have a considerable effect on the mechanical behavior of fabric reinforcements [29–32]. Lebrun et al. [31] studied the in-plane shear deformation of comingled 2x2 twill woven fabrics at elevated temperatures using the bias extension test. It was found that the fabric resistance to shear deformation decreased with increasing temperature due to softening of the comingled thermoplastic fibers. Khan et al. [33] studied the shear deformation of dry carbon fiber 2×2 twill weave fabric at elevated temperatures. Measurements of fabric shear angle during the bias extension tests demonstrated that the degree of inter-yarn slippage increased with increasing temperature. To the best of the authors knowledge, there have been no reported studies that focused on characterizing the deformability of UD-NCFs at elevated temperatures.

During a forming process fabrics may undergo various coupled deformation modes, including in-plane shear and tension and out-of-plane compression and bending [19,34]. Characterizing the formability of fabrics under controlled conditions can provide valuable insight on the mechanisms that influence the formation of defects during draping, while also providing data that can be used to validate corresponding draping simulation models. Several types of forming punch geometries have been adopted in the literature to study the formability of different reinforcement fabrics, with the most common being hemispherical and flat. The hemispherical punch has become a benchmark for studying the formability of many fabric reinforcements [35–37], including more recently for UD-NCFs [4]. Although often used for validating draping simulation models, draping tests involving hemispherical punches have also been used to induce mixed-mode deformations and multiaxial strain states in fabrics to study the influence on defect formation. Flat punches have not been extensively adopted in the literature [38] and have not been employed for UD-NCFs. Flat punches are cylindrical in shape and comprised of relatively sharp corners that contact the fabric specimen during a draping test. The flat punch geometry can induce distinct deformation modes and strain states in fabrics when compared to a hemispherical punch, and may be representative of a deep drawing preforming process.

A review of the current literature has revealed that few studies have investigated and aimed to fully understand the deformation response of heavy-tow UD-NCFs, while few studies have characterized their formability under industrially relevant process conditions that involve biaxial tension and elevated temperatures. To address these important gaps in the literature, the main objective of the present study was to assess and link the local deformation mechanisms and macroscopic deformation response of a heavy-tow tricot stitched carbon fiber UD-NCF under deformation modes experienced during forming operations (i.e., in-plane shear and biaxial tension). The local interactions between the tows and stitching during off-axis extension and biaxial loading captured through optical imaging and strain measurements, and their influence on the macroscopic deformation, were considered. Biaxial tension tests with various displacement ratios were performed at elevated temperatures to investigate the influence of temperature on the coupled orthogonal tensile deformation modes of the UD-NCF. One of the key elements of this study was the use of digital image correlation (DIC) to measure the local strains in the stitching segments as well as the full field strains of the fabric. The formability of the UD-NCF was also investigated during single layer forming experiments using both flat and spherical punches. The mixed-mode deformations during forming of the fabric, including localized shear, were assessed and correlated to the observed defects.

2. Fabric Reinforcement Material

A commercially available UD-NCF, namely Zoltek™ PX35-UD300, was investigated. The heavy-tow fabric was comprised of 5 mm wide tows each containing 50,000 PX35 carbon fiber (CF) filaments. The tows were aligned parallel to each other and stitched together with polyester yarn (76 dtex) in a tricot pattern (Fig. 1). The supporting glass fiber (GF) yarns (34 dtex) were aligned perpendicular to the CF tows, positioned between the CFs and the polyester stitching (Fig. 1). A light thermosetting binder powder, that was intended to cure during fabric forming, was uniformly distributed on the stitching side of the fabric. The total fabric areal density was 333 g/m^2 with the carbon fiber tows accounting for 92.8% of the total weight. All test specimens used in this study were cut from one roll of the UD-NCF fabric.

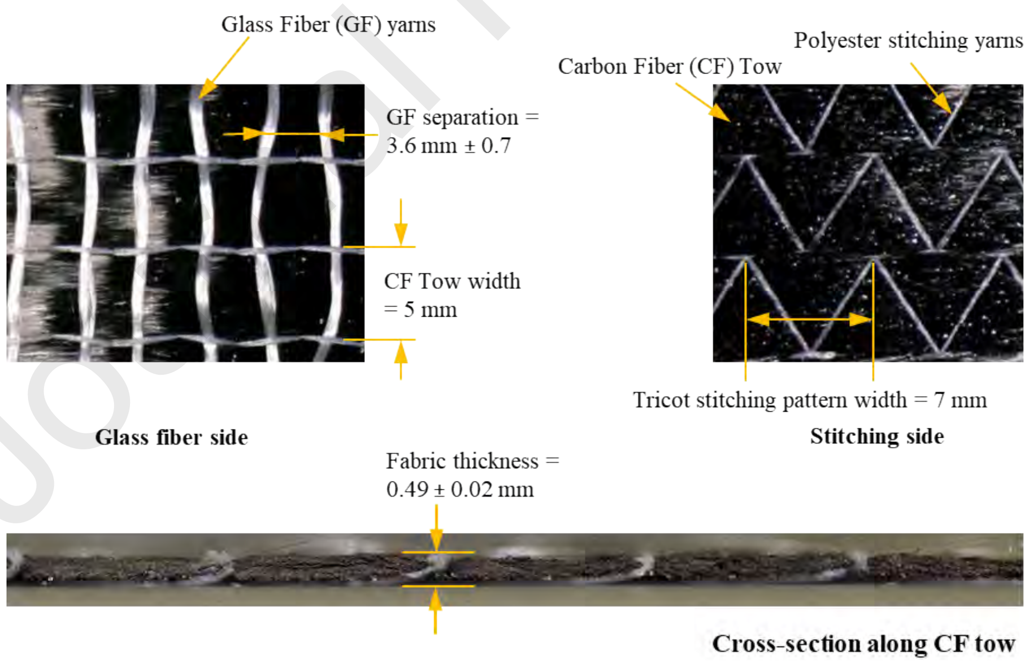

Fig. 1. Images of Zoltek™ PX35-UD300 unidirectional non-crimp fabric illustrating the architecture of the fabric and the components.

3. Experimental Setup

The main features of the characterization tests for in-plane shear and biaxial tension deformation are first presented, followed by details of the draping test setup and the digital image correlation (DIC) techniques used to measure specimen deformation.

3.1. Uniaxial Off-axis Extension Test

UD-NCF specimens for the off-axis extension tests were rectangular with free length L_o = 320 mm and width l_o = 160 mm, resulting in a free length/width ratio of $\lambda = 2$ (Fig. 2a). The carbon fiber tows were oriented at 45° bias to the direction of the applied tension load. All tests were conducted at room temperature on an MTS servo-hydraulic test frame fitted with a Flex-Test SE controller, a 2.2 kN OMEGA LC412-500 load cell and custom fixtures as described in [39] (Fig. 2b). A constant displacement rate of 1 mm/s was used for all performed tests. A digital camera was also used to acquire images for post-processing and measurement of the shear angle distribution using DIC technique (see Fig. 2b and details in Section 3.5). The shear strain for the off-axis extension specimen was calculated using an analytical method [17] that assumes the fabric specimen deforms in simple shear (Fig. 2c). With the longitudinal fabric direction oriented along the line OP, a correlation between an imposed displacement *D* with the angle *w* is:

$$w = sin^{-1}\left(\frac{\sqrt{2}}{2} \cdot \frac{1}{1 + \frac{D}{L_0 - l_0}}\right) \tag{1}$$

Subsequently, the shear angle can be computed as a function of the angle between the longitudinal fabric direction and the loading direction as [16]:

$$\gamma_{ss}(w) = {}^{\pi}/_{2} - w - sin^{-1}\left(\frac{1}{\sqrt{1 + \frac{1}{sin(w)^2} - \frac{2}{tan\,(w)}}}\right) \tag{2}$$

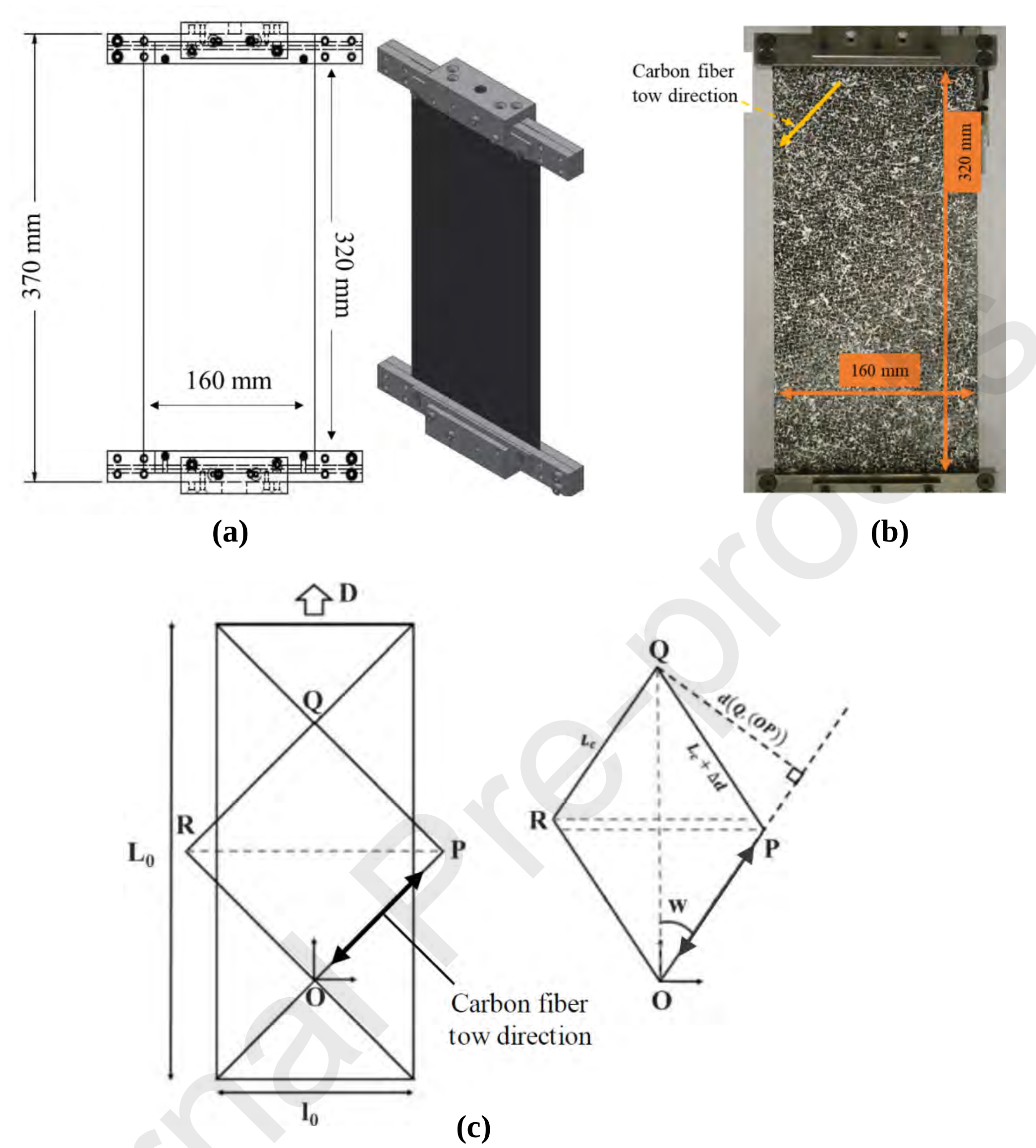

Fig. 2. Off-axis extension test setup: (a) specimen dimensions and clamping system, (b) clamped specimen with applied speckle pattern, and (c) off-axis extension test simple shear deformation approximation [17].

3.2. Picture Frame Test (PFT)

In contrast to the off-axis extension test that provides an assumed simple shear deformation, PFTs were performed to characterize the behavior of the fabric under assumed pure shear deformation. The dimensions of the PFT specimens were comprised of a 170 mm by 170 mm gauge section area with a custom picture frame fixture used to clamp the specimen (Fig. 3a) [39].

Journal Pre-proofs

The fixture was mounted to the same test frame used for the off-axis extension tests from the hinge points (Fig. 3b), enabling application of a displacement on joint A through the crosshead of the test frame (Fig. 3a). The aluminum fixture was designed to accommodate a maximum shear angle of 50°. All tests were conducted at room temperature with a constant displacement rate of 1 mm/s. A digital camera was also used to capture images of the specimen for DIC post-processing.

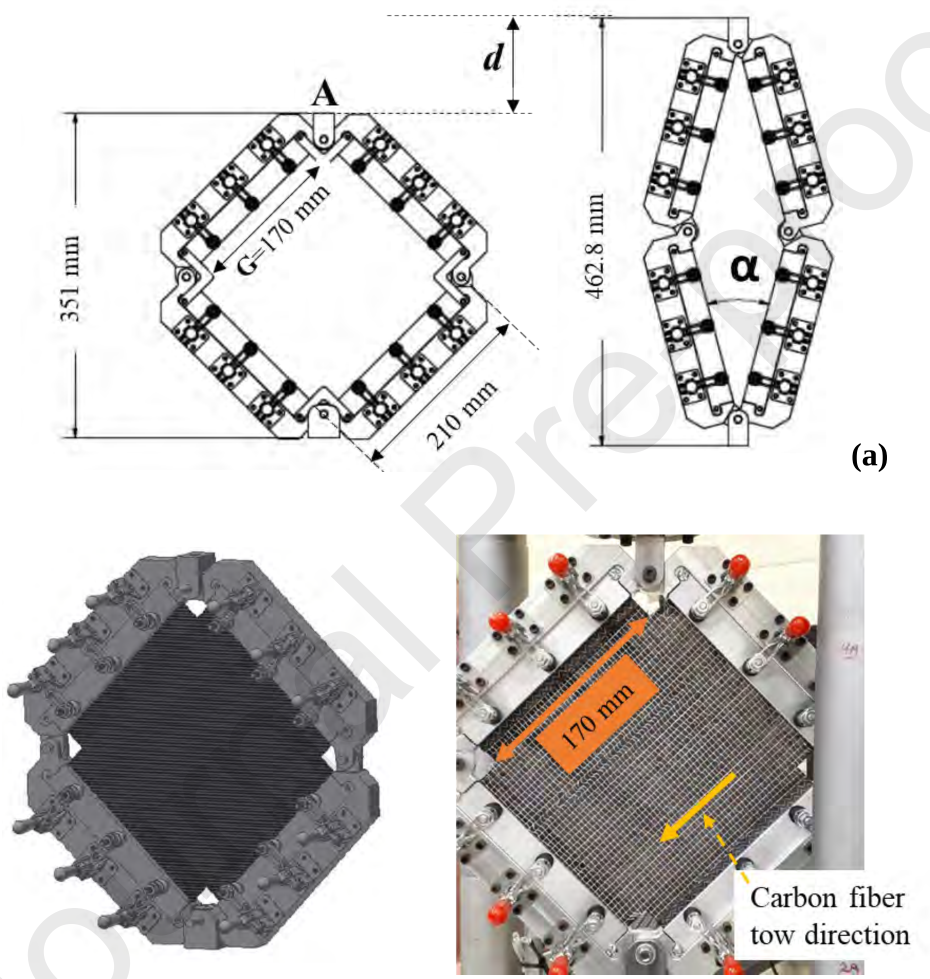

(b)

Fig. 3. (a) Schematic representation of the custom picture frame fixture used with mounted specimen, and (b) picture frame test setup prior to load application.

Journal Pre-proofs

The fabric shear angle (γ) is related to the applied displacement (d) by the correlation of Cao et al. [21]:

$$\gamma[deg] = -0.021d^2 + 2.689\, d\, [mm] \tag{3}$$

The shear force per unit width of the frame side is defined as:

$$F_{sh} = \frac{F^*}{2G\cos\frac{\alpha}{2}} \tag{4}$$

where F^* is the scaled force applied to the specimen at point A that accounts for the recorded displacement from the testing frame, G is the width of the gripped side of the sample, and α is the frame angle (see Fig. 3) which can be related to the shear angle by $\gamma = \frac{\pi}{2} - \alpha$. The force F^* is calculated from the net force applied to the empty frame, F, by:

$$F^* = k_f F \tag{5}$$

where k_f is a coefficient calculated after analyzing the kinematics of the frame as:

$$k_f = 2.522 * 10^{-4} d^2 + 4.453 * 10^{-3} d + 0.1176 \tag{6}$$

Substituting Eqn. (5) into Eqn. (4), it follows that:

$$F_{sh} = \frac{k_f F}{2G\cos\frac{\alpha}{2}} \tag{7}$$

3.3. Biaxial Tension Test

Biaxial tension tests were performed using a custom device equipped with 12 independent jacks along two orthogonal axes (Fig. 4a). The jacks were connected by hinges to allow self-alignment with the loading direction. Each jack had a brush-less motor equipped with an absolute encoder and coupled with a planetary gearbox to transform rotational into linear motion through a ball screw mounted on the axis. The jacks slid on two adjacent rails to allow for transversal displacements along the direction orthogonal to the load. The maximum displacement rate and stroke of the device were 240 mm/min and 512 mm respectively, with a displacement accuracy of 0.05 mm. Each jack comprised a load cell with a maximum capacity of 15 kN. Displacements were applied along the two orthogonal directions of a cruciform specimen (Fig. 4b), which was mounted at the center of the frame. The loading system allowed for application of a biaxial strain field at

Journal Pre-proofs

the center portion (100 x100 mm^2) of the specimen, which was measured using DIC (Section 3.5). Tests were performed at both room temperature and an elevated temperature of 95 ± 3 °C. A thermal chamber integrated with the custom biaxial testing device was used for the elevated temperature tests. The double ventilated chamber had a temperature range of -40°C – +200°C.

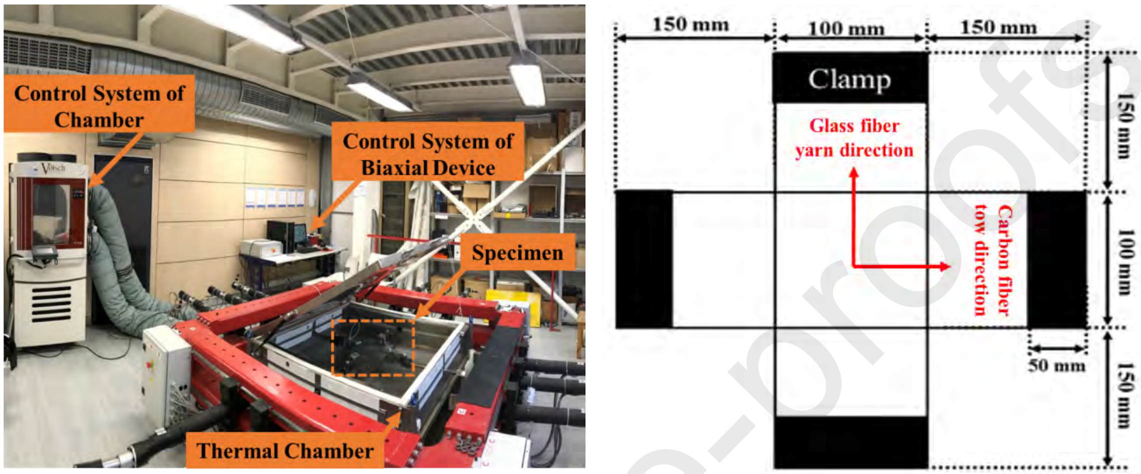

(a) (b)

Fig. 4. (a) Biaxial tensile device and (b) dimensions of the biaxial tensile specimen.

The cruciform specimens had arms with a width of 100 mm (Fig. 4a). A pair of tabs were glued to the clamping zone of each arm of the specimen using 3M-3430 epoxy adhesive. The biaxial tests were performed with different longitudinal (carbon fiber tow direction) to transverse (glass fiber yarn direction) displacement rate ratios, R, namely equibiaxial (R=1, with a displacement rate of 1 mm/min), disproportional (R=0.5 and R=2, with longitudinal displacement rates of 0.5 mm/min and 2 mm/min respectively, while the transverse rate of 1 mm/min) and transverse uniaxial (R=0, with a displacement rate of 1 mm/min). A wide range of biaxial displacement ratios were considered since the fabric may experience these ratios during forming operations.

3.4. Forming Processes

The set-up illustrated in Fig. 5 was adopted to study the formability of the UD-NCF. Single-layer draping tests were performed using a servo-hydraulic MTS formability press fitted with an MTS 407 controller (Fig. 5c). Fabric specimens with dimensions of 200 mm by 200 mm were positioned with the CF tows oriented as in Figs. 5a and 5b. A 50 mm radius hemispherical punch and a 50.5 mm radius flat punch were used to drape the fabric, while a steel ring with a 125 mm inner diameter, 20 mm width, 4 mm thickness and a mass of 259 grams was used to hold the fabric onto the die during draping (Figs. 5a and 5b). Tests were performed at room temperature and under quasi-static conditions with a vertical punch speed of 0.25 mm/s. The deformation of the fabric during forming was measured by a 3D DIC system (Section 3.5).

Journal Pre-proofs

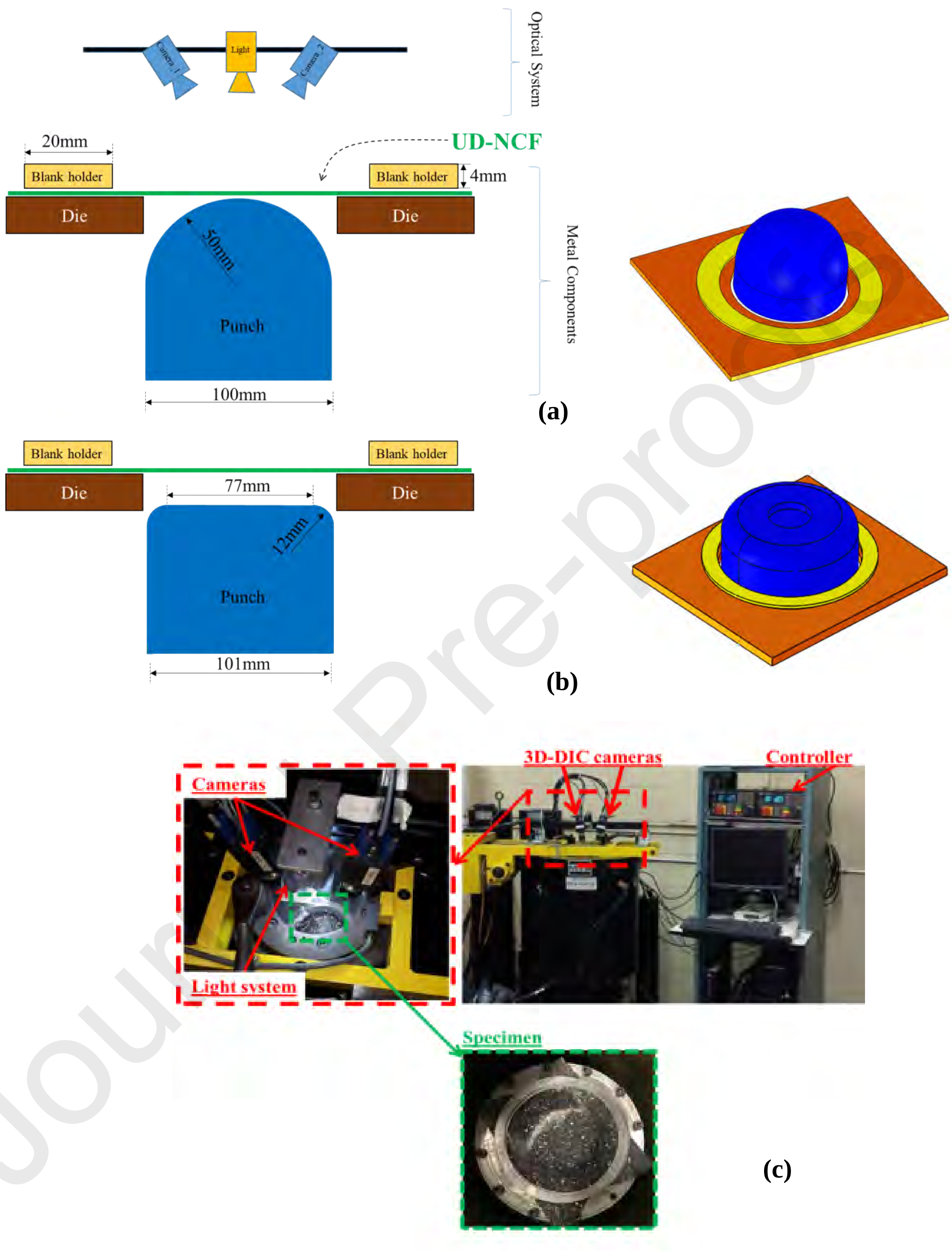

Fig. 5. Schematic of draping tests with (a) hemispherical punch, and (b) flat punch. (c) Draping test setup on MTS formability press.

3.5. Measurements by Digital Image Correlation

The two-dimensional DIC software VIC-2D 2009 (Correlated Solutions Inc.) was used to process images captured during the fabric characterization tests described in Sections 3.1, 3.2 and 3.3. A single Nikon D3200 camera fitted with a Nikon DX Zoom Nikkor 28-55 MM lens positioned perpendicular to the surface of the specimen was used to capture deformations throughout the full specimen surface area at 30 frames per second. It should be noted that for the fabric characterization tests performed in this study, image capturing was limited to load levels where the fabric was subjected to in-plane deformations, thus enabling the use of 2D DIC. Analysis was performed on the complete test specimen surface to generate strain contour plots, and in 50×50 mm^2 (≈200×200 $pixel^2$) regions of interest (ROIs) to record average strain magnitudes. For the computation of the Green-Lagrange strain components, a subset size of 55 pixels, a step size of 5 pixels, a strain filter size of 17, and a typical resolution of 0.25 mm/pixel were used. To increase the correlation capacity of the system given the large deformations expected, the incremental correlation option was activated. Concerning the fabric specimen preparation, the surface was randomly speckled with white oil-based paint to provide a clear contrast with the fabric. During performed in-plane tests, the speckles did not notably influence the deformation response of the fabric and there were no issues with decorrelation, as was reported in [16].

Additionally, a 3D DIC system was used to measure and analyze deformation of the fabric specimens during forming tests. A pair of 17 mm focal length lenses operated at a frame rate of 30 frames per second were used to capture the deformation images. Vic 3D 8 software was employed for analysis using a step size of 5 to 11 pixels, a subset size of 31 to 55 pixels and strain filter size of 9. The same oil-based paint technique was used to speckle the specimen surface, with no decorrelation issues observed.

4. Results and Discussion

4.1. Uniaxial Off-axis Extension Tests

Three repeated off-axis extension tests were performed to capture the shear deformation of the UD-NCF. A comparison of the calculated shear angle using the theoretical kinematic relationship defined by Eq. (3) with that obtained directly using DIC at the center of the specimen (average over ROI) revealed a good correlation up to a shear angle of 20° (Fig. 6a). Beyond 20° the theoretical prediction of shear angle was underestimated due to the simple shear assumption, which does not consider the influence of local deformation mechanisms of the fabric, and further evidenced in the force-shear angle response (Fig. 6b). The force-shear angle plots also revealed the expected three-stage response of the fabric. During the initial stage (up to approximately 5° shear angle) the fabric exhibited a high stiffness and resistance to shear deformation due to the extension of the stitching yarns segments and the resistance to carbon fiber tow rotation cause by friction with the stitching yarns (Fig. 7a). During the second deformation stage (shear angle of 5°-25°), the shear stiffness of the fabric decreased as the carbon fibers tended to rotate towards the loading axis once friction with the stitching was overcome (Fig. 7b). Beyond a shear angle of 15°, the width of the carbon fiber tows began to decrease due to compression induced by the stitching yarns, which promoted inter-tow gapping and sliding [39] and further reduced the fabric shear stiffness (Fig. 7b). During the final deformation stage (shear angle >25°), a rapid increase in stiffness can be explained by the alignment of the stitching yarns with the loading direction and their extension. The stitching web restricted further CF tow rotation, which caused an increase in shear stiffness and shear locking to begin (Fig. 7c). The clamping condition of the off-axis test and the exhibited local deformation mechanisms during the third stage may be the cause of discrepancy between the calculated and measured shear angles, revealing that the theoretical approximation is not valid during the third stage of deformation. The shear angle distribution captured on the test specimen at a load level of 40 N during the third stage of deformation (Fig. 6c) revealed two distinct regions as was described in [4,16]. Region A consisted of a high degree of shear deformation, while region B exhibited limited shear deformation.

Journal Pre-proofs

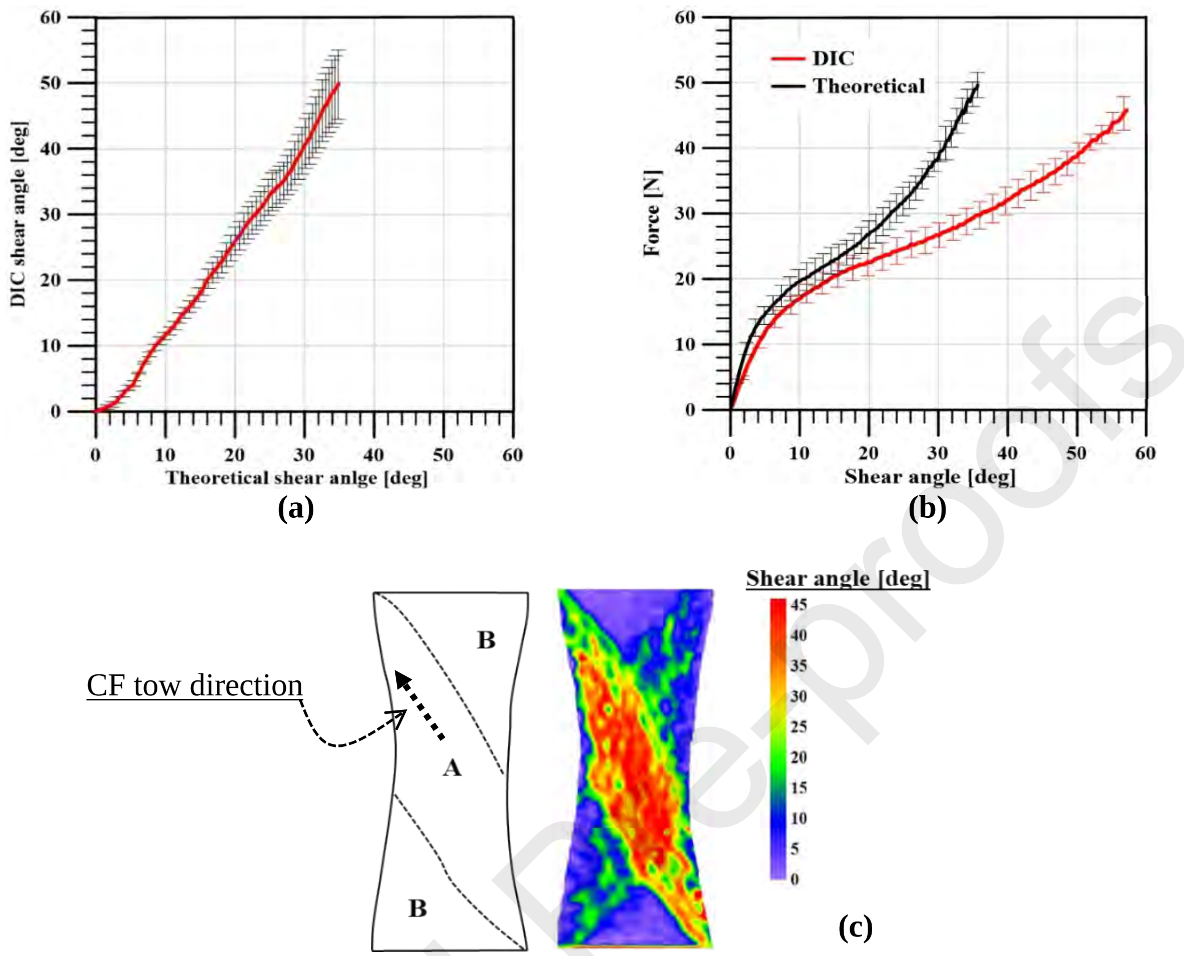

Fig. 6. Off-axis extension test results shown as average of three test specimens with error bars representing scatter: (a) comparison of DIC measured (average over ROI) and theoretical shear angle, (b) force-shear angle response, and (c) deformed specimen schematic and contour plot of the DIC measured shear angle distribution at an applied shear force of 40 N (third stage).

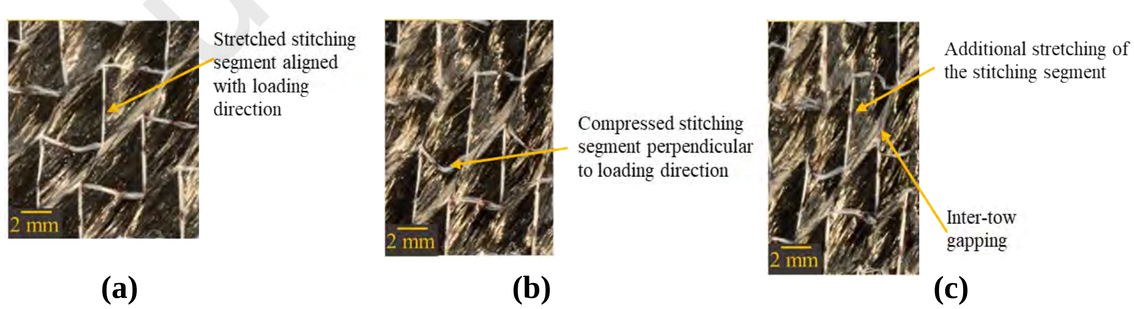

Fig. 7. Images of the stitching side of a UD-NCF specimen during the 45^0 off-axis extension test captured at three different shear angles in the ROI: (a) < 5^0, (b) at 15^0, and (c) > 25^0.

The deformation of the stitching yarns played an important role in the in-plane shear deformation of the UD-NCF during the off-axis extension tests, which warranted further investigation. The deformation of adjacent individual stitching yarn segments was measured at the center of the off-axis extension specimens using captured optical images (see Stitch_1 and Stich_2 in Fig. 8a). The shear deformation of the fabric caused one stitching yarn to extend (Stitch_1), while the adjacent stitching yarn compressed (Stitch_2) (Fig. 8c). The force-axial strain response of the stitching yarns also exhibited three deformation stages, with a rapid increase in the strain during the first and third stages and a more gradual increase in strain during the second stage (Fig. 8b). This is an important result since a clear link between the local deformation of the stitching yarns and the exhibited macroscopic deformation of the fabric was demonstrated (compare Figs. 6b and 8b).

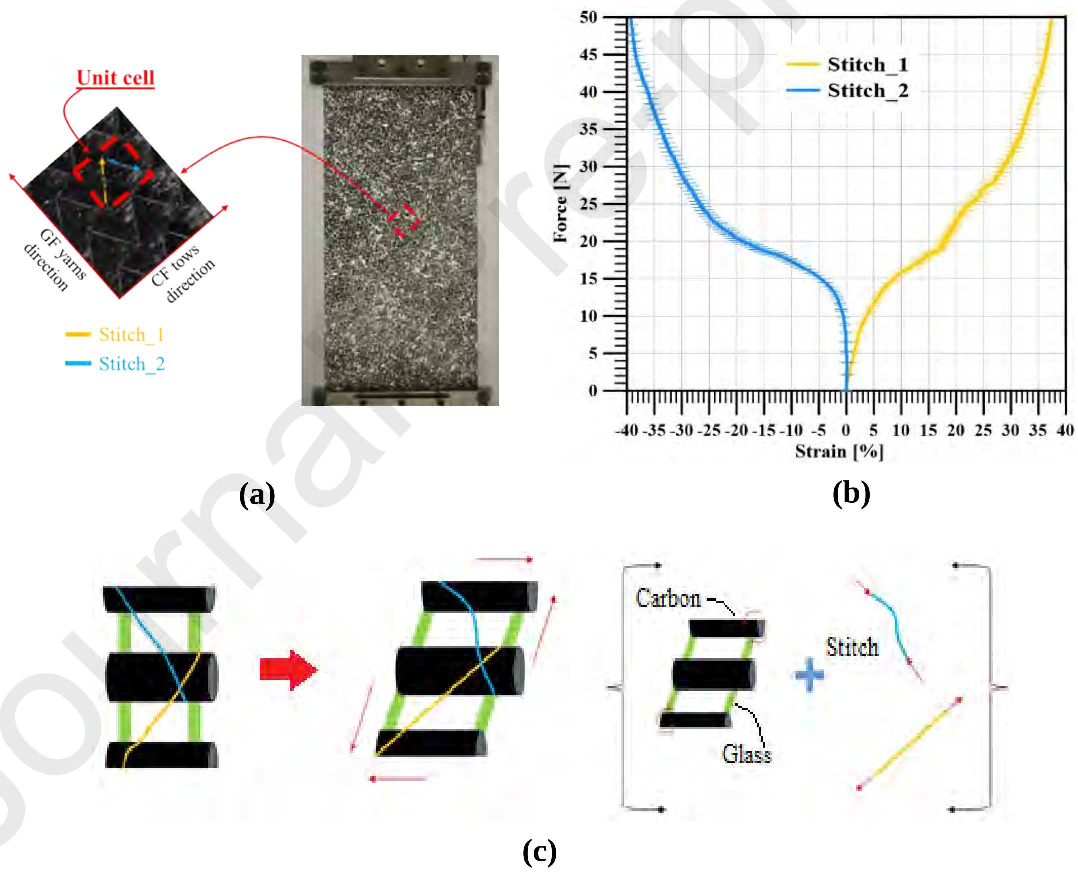

Fig. 8. Optical strain measurement for stitching segments during an off-axis extension test: (a) analyzed fabric unit cell containing Stitch_1 and Stitch_2, and (b) force vs. axial strain for Stitch_1 and Stitch_2 (test results shown are an average of three test specimens with error bars representing scatter). (c) Sketch of the fabric shear deformation mechanism at the stitch level.

Journal Pre-proofs

4.2. Picture Frame Tests

The shear strain response of the fabric was also studied by performing three repeated picture frame tests, under the hypothesis of ideal and homogeneous pure shear deformation. The measured shear angle in the ROI at the center of the specimens using DIC revealed a slight inhomogeneous shear angle distribution (Fig. 9), which was caused by variations in the local deformation of the fabric. The reported shear angle in subsequent plots was taken as the average over the ROI of the specimens.

The normalized shear force vs. shear angle response revealed three stages of deformation (Fig. 10), as was observed for the off-axis extension tests. Note, the procedures described in [21] and [40] for calculating the normalized shear force for the off-axis extension tests and PFTs, respectively, were adopted in this study. During the first stage (shear angle <5°), local stitching-CF tow friction and stretching of the stitching segments caused restricted tow rotation and resulted in a higher shear stiffness (Fig. 11b). Measurement of the stitching segment tensile strain is shown in Fig. 12. The second stage of deformation (up to a shear angle of about 25°) showed a reduced fabric shear stiffness, which started when the friction between the CF tows and stitching was overcome (Fig. 11c). With further increase of the shear angle during the third stage, the observed increase of the stiffness was mainly connected to contact of the tows during lateral compression of the fabric as well as to the overloading of the stitching (see tensile strain in Fig. 12b).

It is important to note that although the shear force-shear angle response captured from the off-axis extension and picture frame tests revealed similar trends, the plots were distinct (Fig. 10). This discrepancy may be in part connected to the different manner the specimens were clamped. The two short sides of the off-axis specimens were clamped, which caused one end of the tows on the short side (Fig. 2a) to be clamped and the other to be free. This allowed for more rotation of the tows, which are not interlaced as in woven fabrics, at higher load level (third stage). In contrast, all sides of the specimen are clamped during the picture frame test, which could constrain the rotation. Furthermore, the off-axis extension tests impose a multiaxial strain state on the specimen, including shear and transverse normal strains, which is distinct from the strain state of the picture frame test specimens [7] . Therefore, the results are expected to be distinct.

Journal Pre-proofs

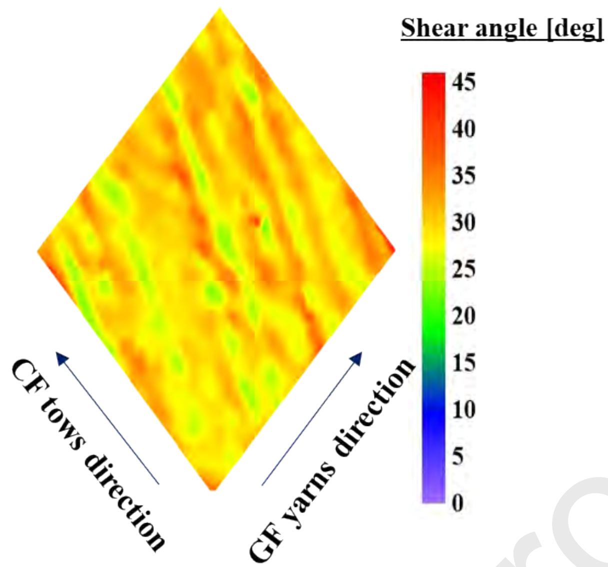

Fig. 9. Contour plot of the DIC measured shear angle distribution in the ROI at the center of a picture frame test specimen at an applied load of 28 N. The CF tow and GF yarn directions are with reference to the undeformed fabric.

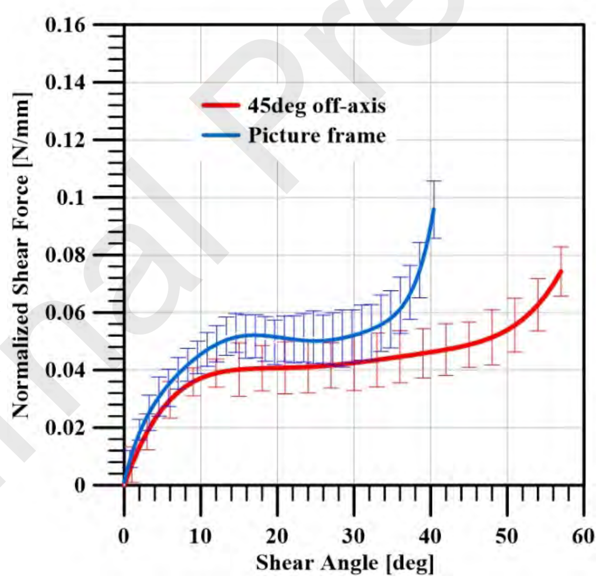

Fig. 10. Normalized shear force-shear angle response using DIC (average over ROI) for picture frame and 45° off-axis extension tests (average of three repeated tests with standard deviation).

Journal Pre-proofs

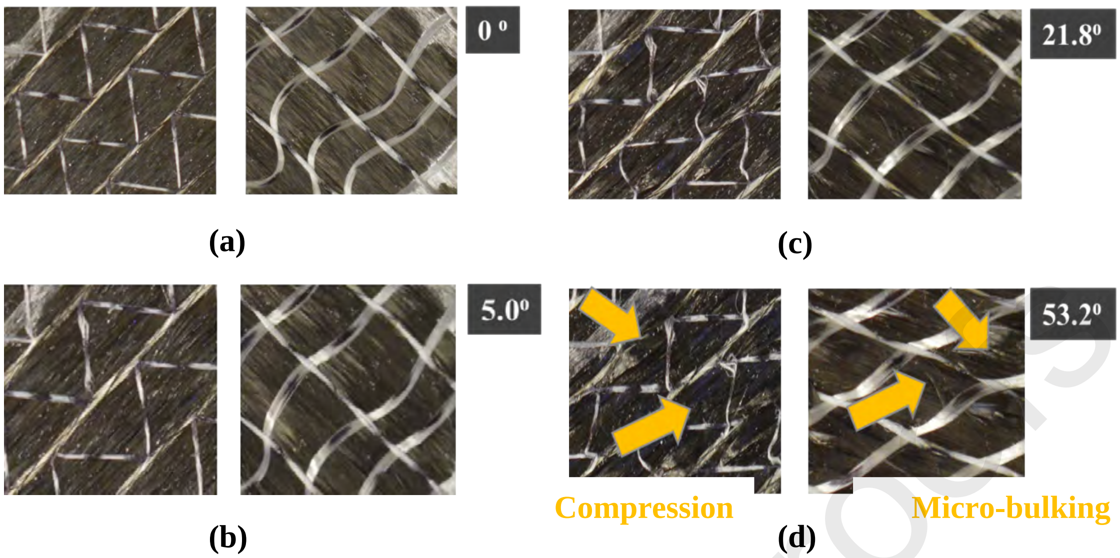

Fig. 11. Local deformation of UD-NCF (stitching and glass sides of the fabric shown) at different frame angles during a picture frame test: (a) 0°, (b) 5°, (c) 21.8°, and (d) 53.2°.

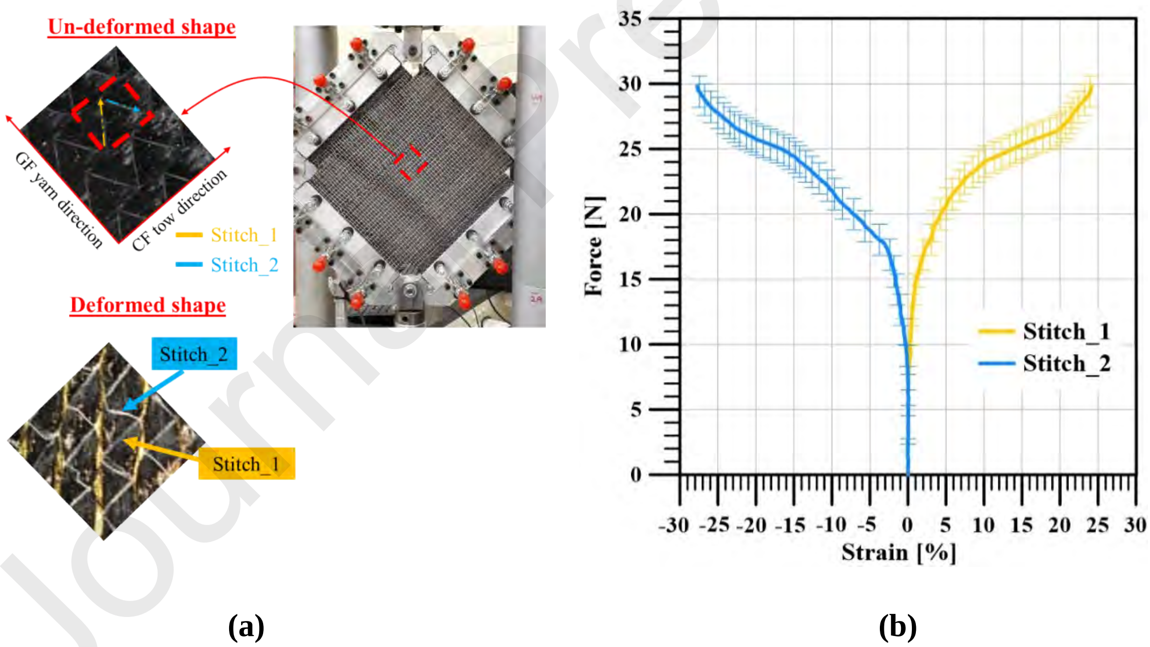

Fig. 12. Optical strain measurements during picture frame test: (a) undeformed and deformed specimen central region showing Stitch_1 and Stitch_2, and (b) force vs. axial strain response for Stitch_1 and Stitch_2 (average of three repeated tests with standard deviation).

4.3. Biaxial Tension Tests

Three repeated tests for each displacement ratio, R, were performed on the cruciform specimens to characterize the biaxial tensile deformation response of the UD-NCF. The scatter in the normalized force-displacement response along the carbon fiber tow direction for different displacement ratios revealed that there was no statistical difference between the data sets prior to 4 mm of displacement (Fig. 13a). However, during this range of displacement the average initial stiffness slightly increased with a decrease in the displacement ratio R, revealing that there was an interdependency between the fabric deformation response along the primary axes. The extension of the initially slack glass fiber yarns with increasing transverse deformation on the fabric may tend to support the in-plane deformation of the stitching yarns and local compression of the carbon fiber tows (Fig. 13c), resulting in a slightly higher resistance to axial deformation. Along the glass fiber yarn direction, the average specimen stiffness did not notably vary with a reduction of the displacement ratio R (Fig. 13b) and may be attributed to the effect of the transverse contraction due to the loading in the carbon fiber tow direction. For R=0, 0.5 and 1, the response along the transverse direction was consistent over the entire range of displacement. Prior to a displacement of 4 mm the magnitude of force was low as a result of extension of the initially slack glass fibers. Beyond 4 mm the glass fibers straightened and the apparent stiffness increased. For R=2 the response was distinct; during the early stages of the test the apparent stiffness was greater than the other displacement ratios, which may be due to the tensioned stitching resisting the deformation of the glass fibers. Overall, the behavior of the UD-NCF under biaxial tension was also influenced by the interactions between the CF tows and stitching.

Fig. 14 depicts the applied load - strain response and maps of the strain component (ε_{11}) in the carbon fiber tow direction for different load ratios. Strain component maps for two displacement ratios (Figs. 14b and 14c) demonstrated that specimens exhibited inhomogeneous local deformations caused by the presence of the stitching filaments and the small gaps it in the fabric. The degree of inhomogeneous specimen deformation decreased with decreasing displacement ratio and can be attributed to the increased fabric stiffness along the carbon tow direction with higher transverse tension, causing more uniform local deformations. For displacement ratios of R = 2 the inhomogeneous deformation persisted throughout the test (Fig. 14b), while for R = 1 the deformations became more uniform at higher applied loads (Figs. 14c).

The behavior of the fabric along the GF yarn direction during biaxial tensile loading is distinct from that along the CF tows due to the lower reinforcement content (see Fig. 15a, three displacement ratios). For displacement ratios of R = 2, the biaxial specimens experienced negative strains (ε_{22}) in the GF direction, despite being loaded in tension. The load in the carbon tow direction generated a transverse contraction (i.e. a compressive strain in the glass yarns), which overtook the transverse tensile deformation imparted by the applied load in the specimen center. Furthermore, an inhomogeneous strain distribution in the GF direction was also observed at the center of the specimens (Fig.15).

Journal Pre-proofs

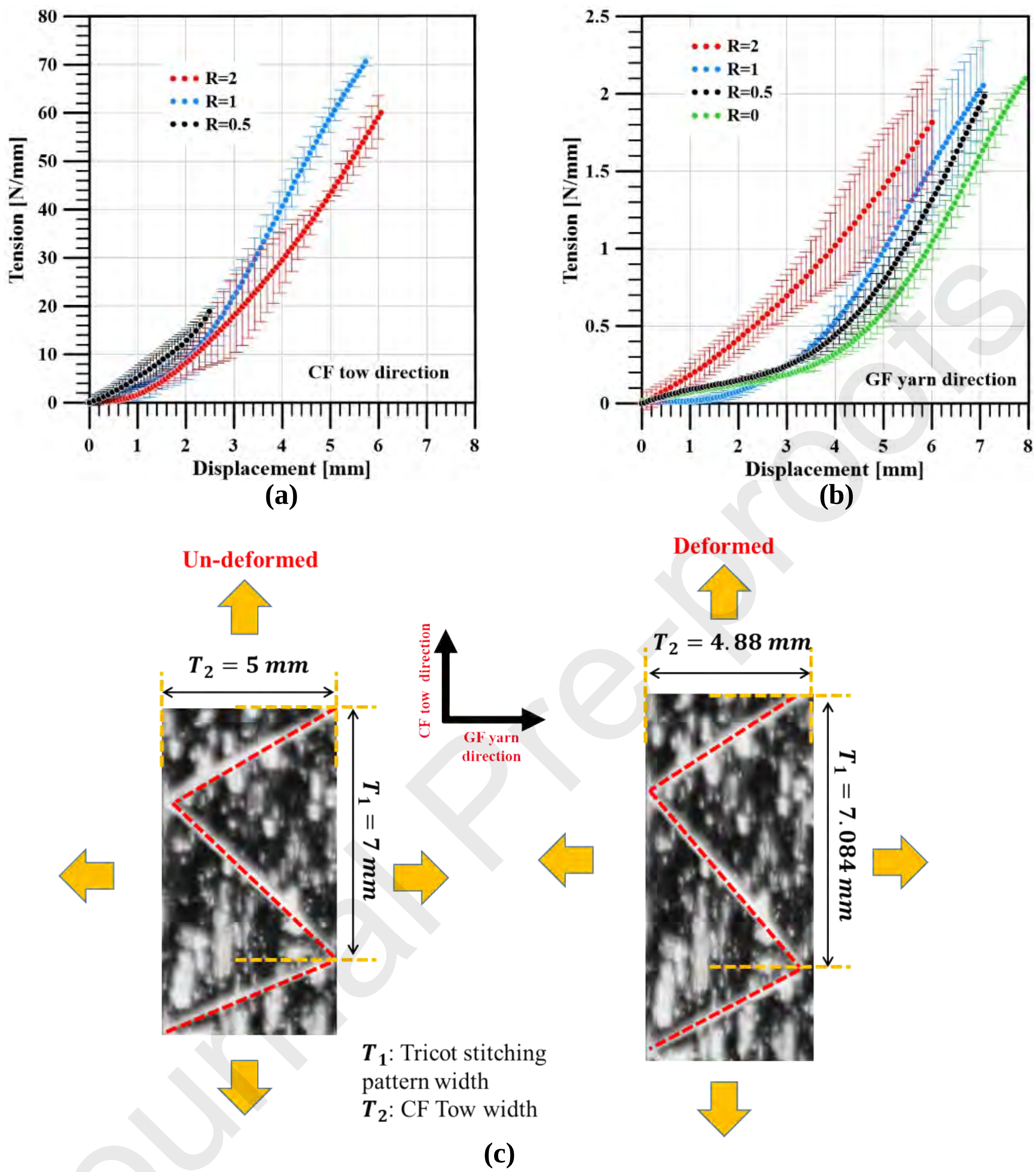

Fig. 13. Biaxial tensile test tension vs. displacement response along the: (a) carbon fiber tow direction, and (b) glass fiber yarn direction. The test results shown are average of three test specimens with error bars representing data scatter, for each indicated displacement ratio. (c) Corresponding undeformed and deformed specimen at the central region (R = 1).

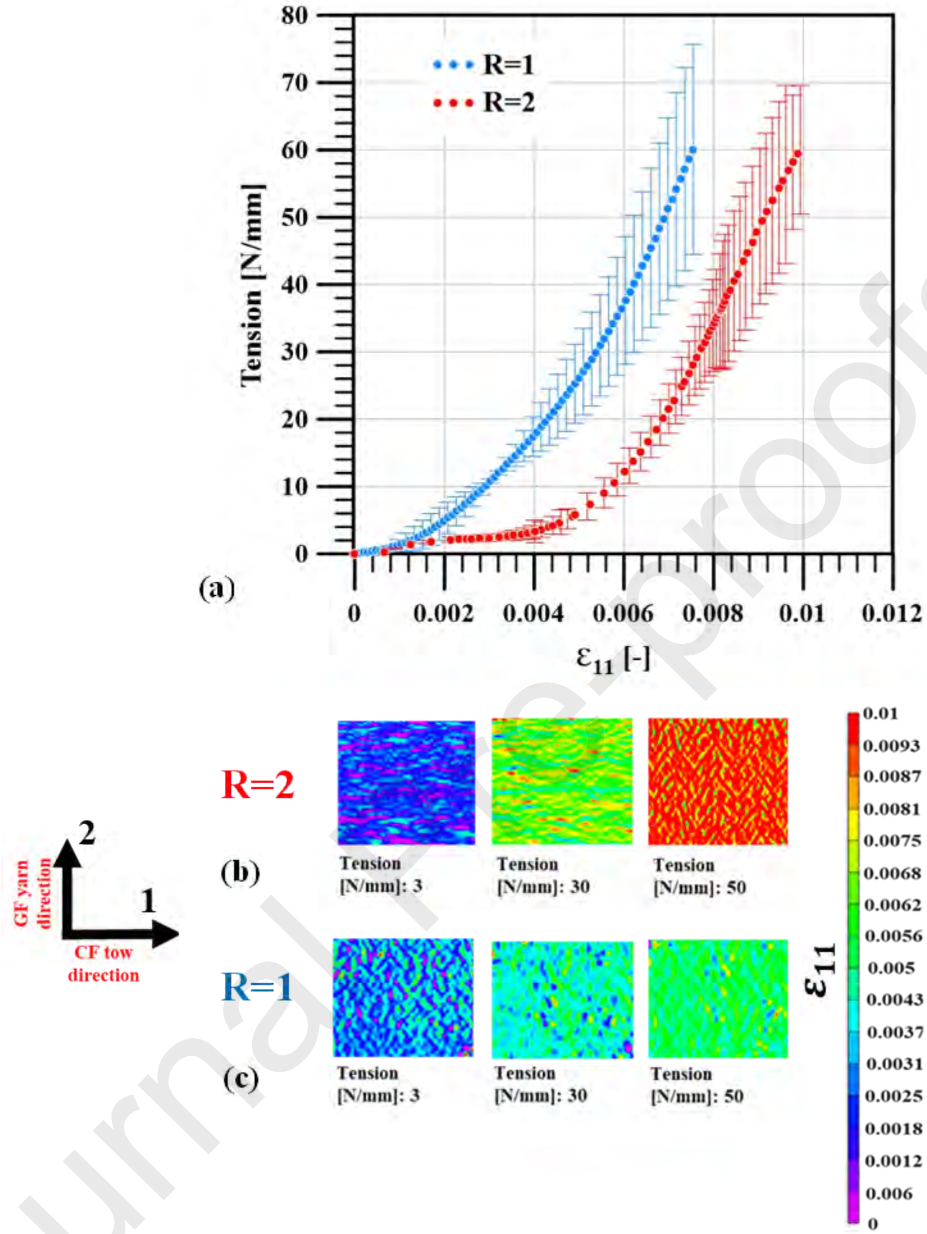

Fig. 14. (a) Biaxial tensile test tension-strain data along the carbon fiber tow direction (strain measured as average in a 50x50 mm^2 ROI at the specimen center, test results shown as average of three repeated tests with error bars representing scatter). Corresponding DIC maps in ROI for normal strain along the carbon fiber tow direction for displacement ratio of: (b) R=2, (c) R=1.

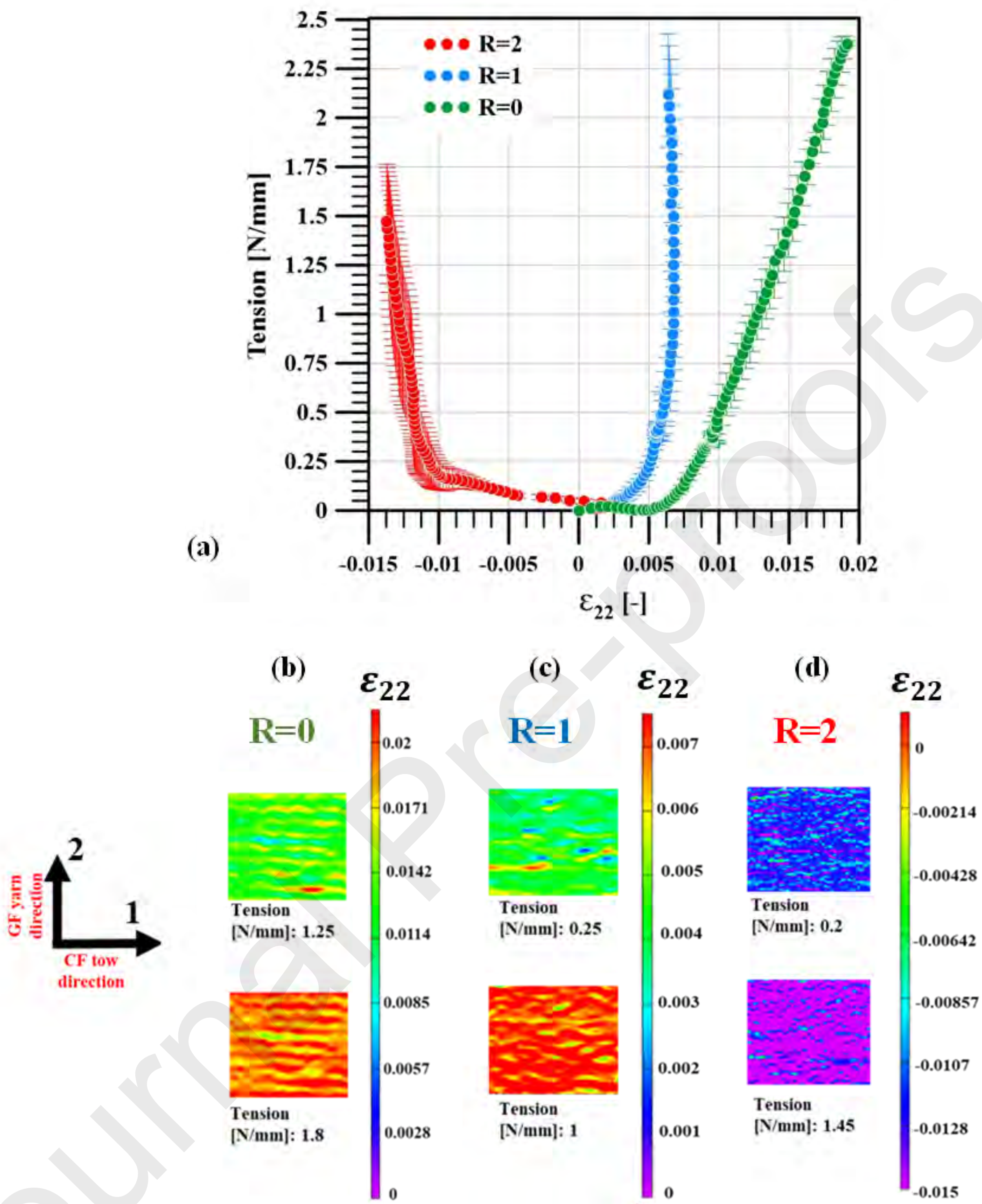

Fig. 15. (a) Biaxial tensile test tension-strain data along the glass fiber yarn direction (strain measured as average in a 50x50 mm^2 ROI at the specimen center, test results shown as average of three repeated tests with error bars representing scatter). Corresponding DIC maps in ROI for normal strain along the glass fiber yarn direction for displacement ratio of: (b) R=0, (c) R=1, and (d) R=2.

Additional biaxial tensile tests were performed at selected temperature of 95±3°C to mimic the conditions of an in-mold preforming process for the UD-NCF. The temperature is below the glass transition temperature of the stitching polyester yarns (on the order of 200°C) and equivalent to the recommended curing temperature of the thermosetting binder powder. A comparison of the biaxial tensile response at room and elevated temperature, for each displacement ratio, demonstrated a consistent behavior of the fabric specimens along both the carbon tow and glass yarn directions (Figs. 16 and 17). The macroscopic fabric response and local carbon fiber tow-stitching interactions were not influenced by the temperatures considered, which is of considerable importance for resin infusion processes for CFRP parts.

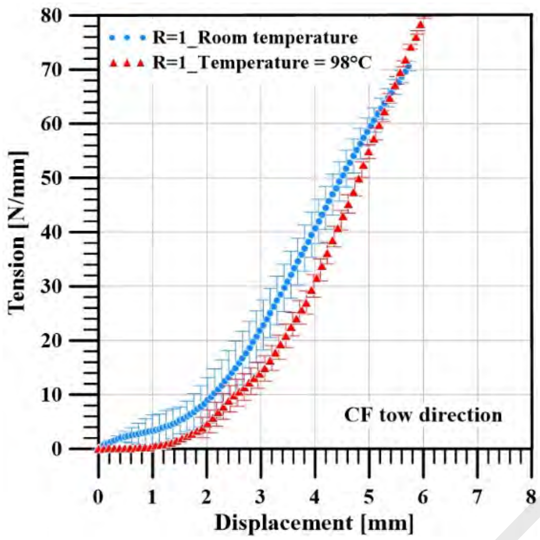

(a)

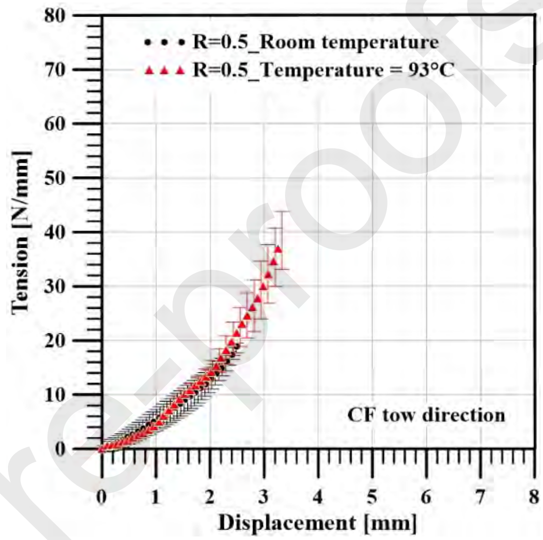

(b)

Fig. 16. Biaxial tensile test tension-displacement response along the carbon fiber tow direction at room and elevated temperature: (a) R=1, and (b) R=0.5. (Test results shown as average of three test specimens with error bars representing scatter)

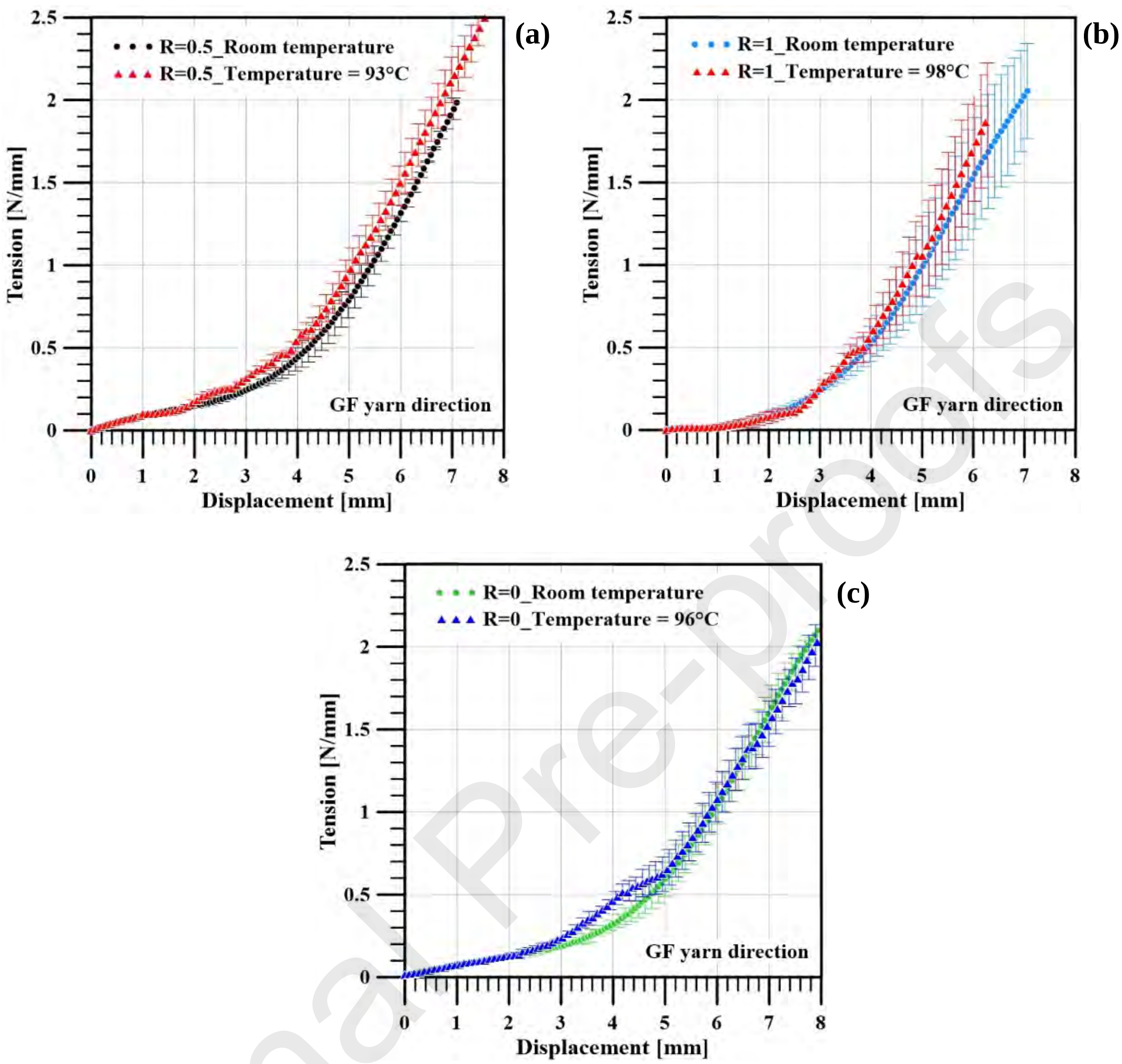

Fig. 17. Biaxial tensile test tension-displacement response along the glass fiber yarn direction at room and elevated temperature: (a) R=0.5, (b) R=1, and (c) R=0. (Test results shown as average of three test specimens with error bars representing scatter)

4.4. Forming Experiments

Two sets of draping tests were performed to investigate the formability, local deformation mechanisms and typical forming defects for a single layer of the UD-NCF, using either a hemispherical or flat punch. Three repeats were performed for both sets of draping tests.

The defects observed on the deformed fabric during the flat punch tests included wrinkles near the blank holder parallel to the carbon fiber tow direction, as well as local CF tow buckling (Fig. 18a). Wrinkling is a macro-scale defect caused by local transverse compressive deformation of the

Journal Pre-proofs

carbon fiber tows and tow gapping, which was primarily driven by the in-plane shear deformation of the fabric (see Fig. 7). Local transverse buckling of the CF tows occurred at the meso-scale between two adjacent stitching yarns, where one stitching yarn was subjected to axial compression, and is also primarily driven by in-plane shear deformation of the fabric (see Fig. 8). Strain maps of the center portion of the fabric (approximately a 30 mm radius directly above the flat portion of the punch), derived using 3D DIC, revealed homogeneous longitudinal (ε_{11}), transverse (ε_{22}) and shear (ε_{12}) strain components at the specimen center as expected (Figs. 18b-18d). It is interesting that the strain state at the specimen center at 27 mm punch displacement was approximately equi-biaxial with $\varepsilon_{11} = \varepsilon_{22} = 1.0\%$ (Figs. 18b and 18c), with homogeneous shear strain (ε_{12}) distribution. Assessment of the shear angle distribution over the top surface of the specimen at a punch displacement of 27 mm revealed that peak shear angles of approximately 20° were located on the cylindrical part of the punch, which could be connected to the observed defects near the blank holder, while the shear angles at the center of the specimen were <3° (Fig. 18e). Although the local shear deformation of the fabric was an important factor driving the observed wrinkling and local CF tow buckling, the combined transverse compressive strains along the GF yarns (ε_{22}) also contributed to macroscopic wrinkling. It should be noted that although bending of the fabric was not considered in this study, this deformation mode would also impact the formation of wrinkles to some extent.

The defects observed during the draping tests with the hemispherical punch were also macroscopic wrinkling and local CF tow transverse buckling, and similarly located close to the blank holder (Fig. 19a). The strain state at the center of the specimen after 27 mm punch displacement was approximately equi-biaxial with $\varepsilon_{11} = \varepsilon_{22} = 2\%$ (Figs. 19b and 19c). However, the region of the specimen with a peak transverse tensile strain was notably larger than that with a peak longitudinal tensile strain (Fig. 19c), which contributed to CF tow separation and stitching failure after 45 mm of punch displacement (Fig. 19f). The shear angle distribution over the surface of the specimens revealed peak shear angles near the blank holder at the locations of the observed defects (Fig. 19a and 19e). The notable transverse compressive strains observed on the specimens at the same locations (Fig. 19c) also contributed to the development of macroscopic wrinkling. It is interesting to note that the shear angles measured for the studied UD-NCF were notably lower in magnitude when compared shear angles measured for other types of fabrics when subjected to similar draping conditions [19, 24, 33]. This implies that the observed local deformation mechanisms (i.e. stitching deformation and interaction with the CF tows) promote an increase in shear stiffness for the NCF, which further shows that the influence of the transverse compressive strains on wrinkle formation is notable at higher punch displacements.

Journal Pre-proofs

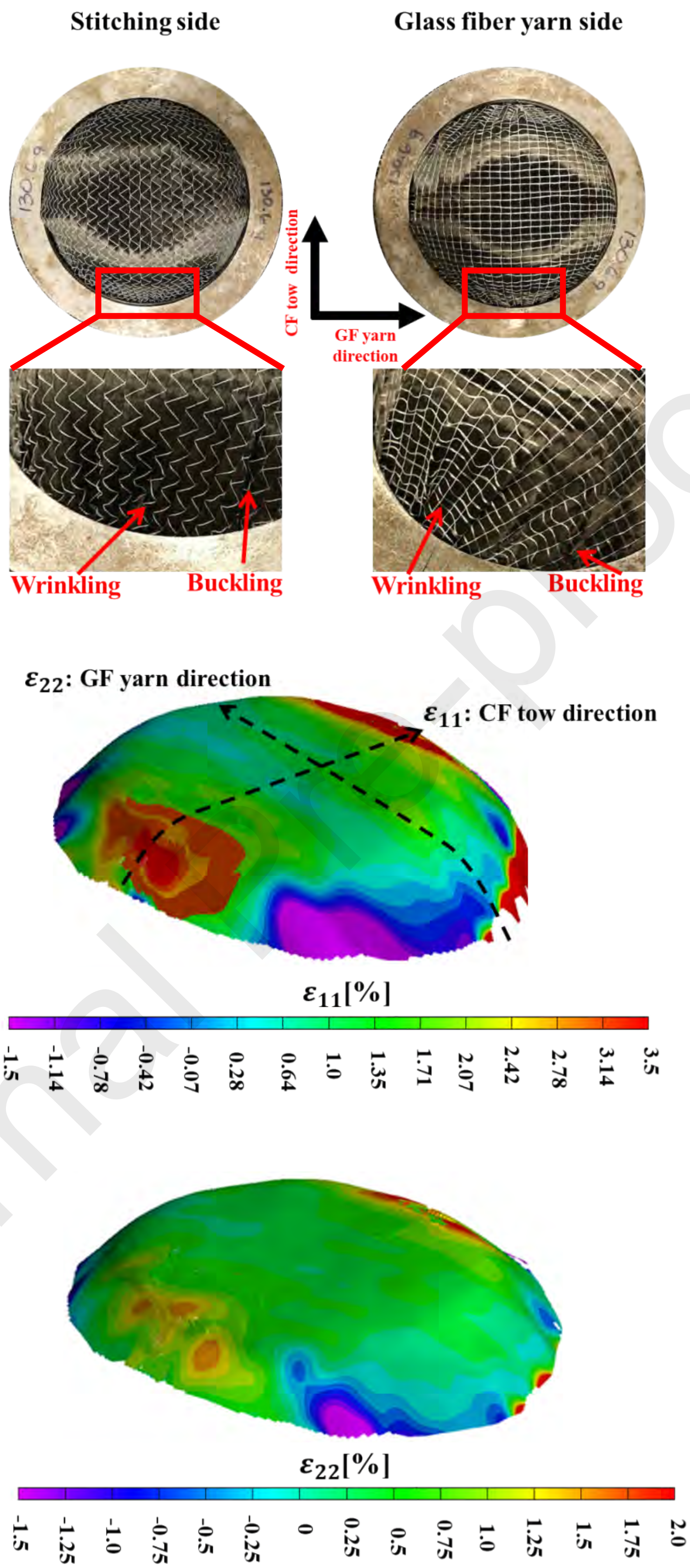
Stitching side
Glass fiber yarn side
CF tow direction
GF yarn direction
Wrinkling
Buckling
Wrinkling
Buckling
ε_{22}: GF yarn direction
ε_{11}: CF tow direction
ε_{11}[%]
-1.5 -1.14 -0.78 -0.42 -0.07 0.28 0.64 1.0 1.35 1.71 2.07 2.42 2.78 3.14 3.5
ε_{22}[%]
-1.5 -1.25 -1.0 -0.75 -0.5 -0.25 0 0.25 0.5 0.75 1.0 1.25 1.5 1.75 2.0

(a)

(b)

(c)

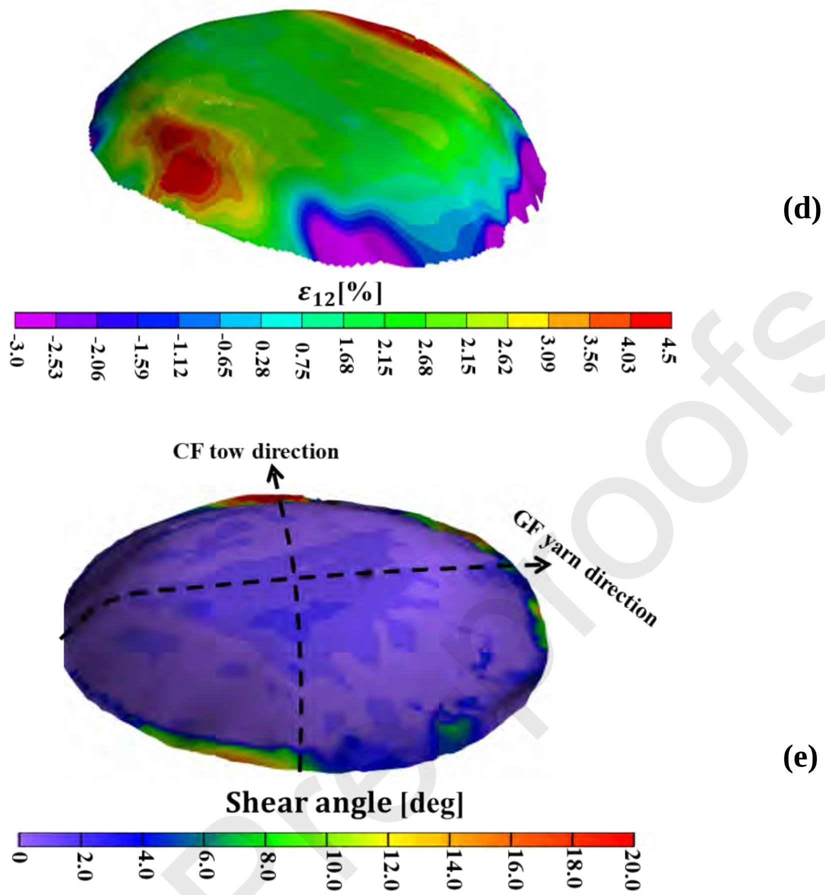

Fig. 18. Deformation of the UD-NCF specimen during flat punch forming at 27mm punch displacement: (a) fabric stitching side and glass fiber yarn side, (b) map of longitudinal strain (ε_{11}), (c) map of transverse strain (ε_{22}), (d) map of shear strain (ε_{12}), and (e) map of shear angle. Note, fabric strain and shear angle maps were captured by DIC at the specimen center above the flat punch.

Journal Pre-proofs

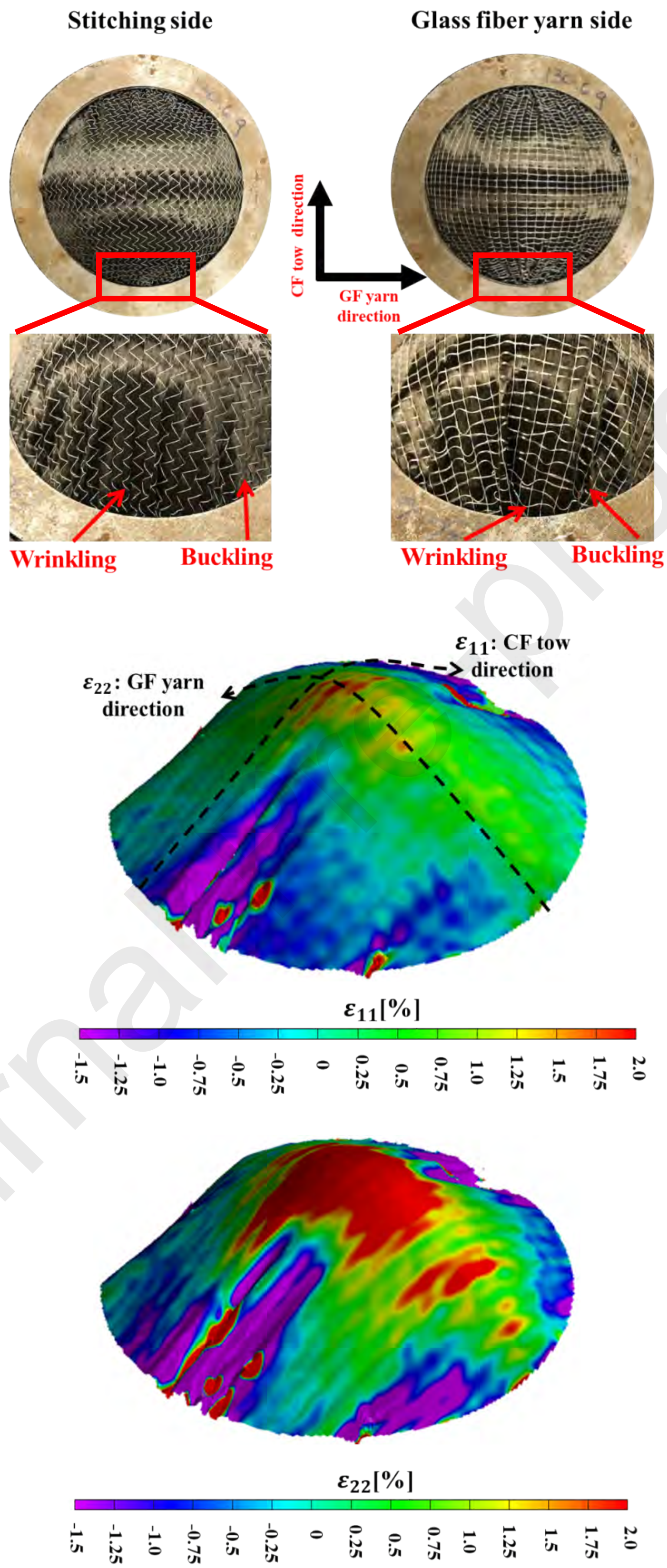

(a)

(b)

(c)

Journal Pre-proofs

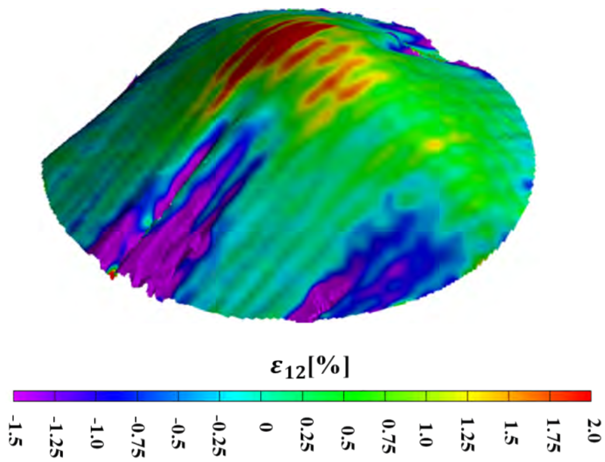

(d)

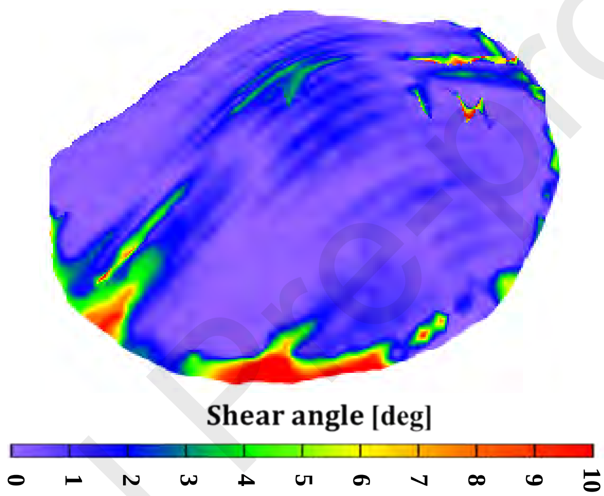

(e)

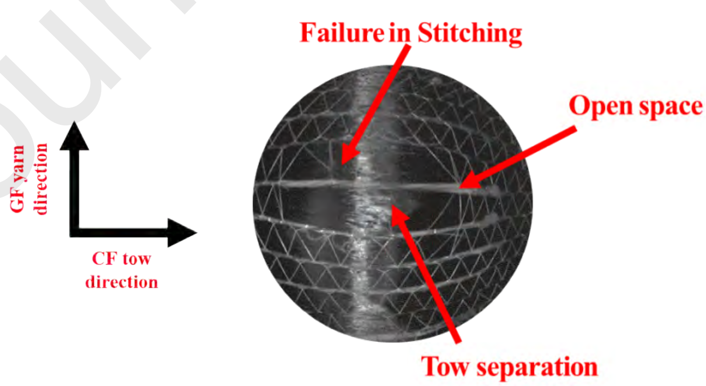

(f)

Fig. 19. Deformation of the UD-NCF specimen during hemispherical punch forming at a punch displacement of 27mm: (a) fabric stitching side and glass fiber yarn side, (b) map of longitudinal strain (ε_{11}), (c) map of transverse strain (ε_{22}), (d) map of shear strain (ε_{12}), and (e) map of shear

Journal Pre-proofs

angle. Note, fabric strain and shear angle maps for the specimen were captured by DIC for the portion of the specimens within the blank holder. (f) Stitching side of fabric specimen at a punch displacement of 45mm.

5. Conclusions

The aim of this investigation was to characterize and link the local deformation mechanisms and macroscopic response of a heavy-tow tricot stitched carbon fiber unidirectional non-crimp fabric (UD-NCF). Off-axis extension, picture frame and biaxial tension tests were conducted to characterize the main fabric membrane deformation modes exhibited during a preforming operation (i.e., in-plane shear and biaxial tension). Biaxial tension tests were also performed at elevated temperatures to study the influence of temperature on the macroscopic deformation of the UD-NCF. In addition, draping tests were performed to study the formability of a single layer of fabric. Digital image correlation (DIC) was used to capture both local strains in the fabric constituents as well as full field strain maps for the fabric specimens.

The in-plane shear deformation tests revealed that the extension/compression of the stitching segments traversing the carbon fiber (CF) tows and the local interactions between the stitching and CF tows directly influenced the exhibited three-stage fabric shear deformation response. More importantly, the measured stitching segment strains during the off-axis extension tests, which are unique results, also exhibited a three-stage response and provided direct evidence of a link between the local deformation mechanisms and the macroscopic fabric response. Biaxial tension tests at different displacement ratios revealed the interdependency of the orthogonal tensile deformation modes of the fabric caused by the interactions between the glass fiber (GF) yarns, stitching segments and CF tows. The quantified data represents another unique and important data set generated in this study. Moreover, biaxial tension tests conducted at an elevated ambient temperature of 95±3°C revealed that temperature did not notable influence deformation response of the fabric. This is an interesting result for industrial applications since the deformation response of the polyester stitching, which notably influenced the biaxial tension response of the fabric, was not affected by the considered temperature which was below the glass transition temperature of the stitching.

The single layer fabric forming tests with both flat and hemispherical punches highlighted that the main defects were local buckling and macroscopic wrinkling of the CF tows. The measured full field shear angle and strain component contours at the final stage of forming, extracted using 3D DIC, showed the interaction of the deformation modes that drove these observed defects (i.e., combined in-plane shear and transverse compression deformation). These critical deformation modes were clearly observed during both sets of forming tests considered and quantified for the first time in this study.

Collectively, the investigation of local deformation mechanisms, macroscopic deformation modes and the fabric formability characteristics provide an improved understanding of the interdependent multi-scale response of the heavy-tow tricot stitched carbon fiber UD-NCF. Specifically, the critical role of the stitching yarn on the deformability and formability of the fabric was captured and the stitching segment strains were quantified. The generated data set and qualitative assessments will also be important for the future development of a fabric constitutive model.

Acknowledgements

The authors thank the Natural Sciences and Engineering Research Council of Canada (NSERC) for supporting this study through funding grant CRDPJ-507776-16. The Advanced Manufacturing Consortium (AMC) of Ontario, and the industry sponsors Honda R&D Americas LLC., Hexion Inc., Zoltek Corp. and LAVAL International are also acknowledged for funding this study. The Textiles HUB of Politecnico di Milano is gratefully acknowledged for providing access to the biaxial experimental device.

References

[1] Swentek I, Beck B, Potyra T, Ugresic V, Henning F. Impact of HP-RTM Process Parameters on Mechanical Properties Using Epoxy and Polyurethane. 14th-Annu. SPE Automot. Compos. Conf. Exhib. ACCE, Novi, MI, USA, September 9-11, 2015, p. 1–10.

[2] Mitschang P. 3 - Structural stitching of non-crimp fabric preforms for composites. In: Lomov SV, editor. Non-Crimp Fabr. Compos., Woodhead Publishing; 2011, p. 67–83. https://doi.org/10.1533/9780857092533.1.67.

[3] Arnold SE, Sutcliffe MPF, Oram WLA. Experimental measurement of wrinkle formation during draping of non-crimp fabric. Compos Part A Appl Sci Manuf 2016;82:159–69. https://doi.org/10.1016/j.compositesa.2015.12.011.

[4] Schirmaier FJ, Dörr D, Henning F, Kärger L. A macroscopic approach to simulate the forming behaviour of stitched unidirectional non-crimp fabrics (UD-NCF). Compos Part A Appl Sci Manuf 2017;102:322–335. https://doi.org/10.1016/j.compositesa.2017.08.009.

[5] Chen S, McGregor OPL, Harper LT, Endruweit A, Warrior NA. Defect formation during preforming of a bi-axial non-crimp fabric with a pillar stitch pattern. Compos Part A Appl Sci Manuf 2016. https://doi.org/10.1016/j.compositesa.2016.09.016.

[6] Sköck-Hartmann B, Gries T. 20 - Automotive applications of non-crimp fabric composites. In: Lomov SV, editor. Non-Crimp Fabr. Compos., Woodhead Publishing; 2011, p. 461–80. https://doi.org/10.1533/9780857092533.4.461.

[7] Schirmaier FJ, Weidenmann KA, Kärger L, Henning F. Characterisation of the draping behaviour of unidirectional non-crimp fabrics (UD-NCF). Compos Part A Appl Sci Manuf 2016;80:28-38. https://doi.org/10.1016/j.compositesa.2015.10.004.

[8] Salvatori D, Caglar B, Teixidó H, Michaud V. Permeability and capillary effects in a channel-wise non-crimp fabric. Compos Part A Appl Sci Manuf 2018;108:41–52. https://doi.org/10.1016/j.compositesa.2018.02.015.

[9] Mallach A, Härtel F, Heieck F, Fuhr JP, Middendorf P, Gude M. Experimental comparison of a macroscopic draping simulation for dry non-crimp fabric preforming on a complex geometry by means of optical measurement. J Compos Mater 2017;51:2363–2375. https://doi.org/10.1177/0021998316670477.

[10] Krieger H, Gries T, Stapleton SE. Shear and drape behavior of non-crimp fabrics based on stitching geometry. Int J Mater Form 2018;11:593–605. https://doi.org/10.1007/s12289-017-1368-1.

[11] Lomov SV. 6 - Deformability of textile performs in the manufacture of non-crimp fabric composites. In: Lomov SV, editor. Non-Crimp Fabr. Compos., Woodhead Publishing; 2011, p. 117–144e. https://doi.org/10.1533/9780857092533.2.117.

[12] Magagnato D, Henning F. RTM molding simulation for unidirectional fiber reinforced composite components considering local fiber orientation and fiber volume fraction. J Sci Alliance Plast Technol 2016;12:136–56.

[13] Krieger H, Gries T, Stapleton SE. Design of Tailored Non-Crimp Fabrics Based on Stitching Geometry. Appl Compos Mater 2018;25:113-127. https://doi.org/10.1007/s10443-017-9603-y.

[14] Mattner T, Wrensch M, Drummer D. Shear behavior of woven and non-crimp fabric based thermoplastic composites at near-processing conditions. Compos Part B Eng 2020;185:107761. https://doi.org/10.1016/j.compositesb.2020.107761.

[15] Harrison P. Normalisation of biaxial bias extension test results considering shear tension coupling. Compos Part A Appl Sci Manuf 2012;43:1546–1554. https://doi.org/10.1016/j.compositesa.2012.04.014.

[16] Trejo EA, Ghazimoradi M, Butcher C, Montesano J. Assessing strain fields in unbalanced unidirectional non-crimp fabrics. Compos Part A Appl Sci Manuf 2020;130. https://doi.org/10.1016/j.compositesa.2019.105758.

[17] Pourtier J, Duchamp B, Kowalski M, Wang P, Legrand X, Soulat D. Two-way approach for deformation analysis of non-crimp fabrics in uniaxial bias extension tests based on pure and simple shear assumption. Int J Mater Form 2019;12:995-1008. https://doi.org/10.1007/s12289-019-01481-8.

[18] Willems A, Lomov SV, Verpoest I, Vandepitte D. Optical strain fields in shear and tensile testing of textile reinforcements. Compos Sci Technol 2008. https://doi.org/10.1016/j.compscitech.2007;68:807-819.

Journal Pre-proofs

[19] Gereke T, Döbrich O, Hübner M, Cherif C. Experimental and computational composite textile reinforcement forming: A review. Compos Part A Appl Sci Manuf 2013;46:1–10. https://doi.org/10.1016/j.compositesa.2012.10.004.
[20] Komeili M, Milani AS. On effect of shear-tension coupling in forming simulation of woven fabric reinforcements. Compos Part B Eng 2016;99:17–29. https://doi.org/10.1016/j.compositesb.2016.05.004.
[21] Cao J, Akkerman R, Boisse P, Chen J, Cheng HS, de Graaf EF, et al. Characterization of mechanical behavior of woven fabrics: Experimental methods and benchmark results. Compos Part A Appl Sci Manuf 2008;39:1037–53. https://doi.org/10.1016/j.compositesa.2008.02.016.
[22] Lomov SV, Boisse P, Deluycker E, Morestin F, Vanclooster K, Vandepitte D, et al. Full-field strain measurements in textile deformability studies. Compos Part A Appl Sci Manuf 2008;39:1232–1244. https://doi.org/10.1016/j.compositesa.2007.09.014.
[23] Buet-Gautier K, Boisse P. Experimental analysis and modeling of biaxial mechanical behavior of woven composite reinforcements. Exp Mech 2001;41:260–9. https://doi.org/10.1007/BF02323143.
[24] Lomov SV, Willems A, Verpoest I, Zhu Y, Barburski M, Stoilova T. Picture Frame Test of Woven Composite Reinforcements with a Full-Field Strain Registration. Text Res J 2006;76:243–252. https://doi.org/10.1177/0040517506061032.
[25] Vanleeuw B, Carvelli V, Barburski M, Lomov SV, van Vuure AW. Quasi-unidirectional flax composite reinforcement: Deformability and complex shape forming. Compos Sci Technol 2015;110:76–86. https://doi.org/10.1016/j.compscitech.2015.01.024.
[26] Ghazimoradi M, Carvelli V, Marchesi MC, Frassine R. Mechanical characterization of tetraxial textiles. J Ind Text, 48, 3–24, 2018. https://doi.org/10.1177/1528083717721920.
[27] Lomov SV. Non-crimp fabric composites: Manufacturing, properties and applications, Woodhead Publishing; 2011;32:4278–88. https://doi.org/10.1533/9780857092533.
[28] Lomov SV, Barburski M, Stoilova T, Verpoest I, Akkerman R, Loendersloot R, et al. Carbon composites based on multiaxial multiply stitched preforms. Part 3: Biaxial tension, picture frame and compression tests of the preforms. Compos Part A Appl Sci Manuf 2005;36:1188-1206. https://doi.org/10.1016/j.compositesa.2005.01.015.
[29] Hufenbach W, Gude M, Böhm R, Zscheyge M. The effect of temperature on mechanical properties and failure behaviour of hybrid yarn textile-reinforced thermoplastics. Mater Des 2011;32:4278–88. https://doi.org/10.1016/j.matdes.2011.04.017.
[30] Wang P, Hamila N, Pineau P, Boisse P. Thermomechanical analysis of thermoplastic composite prepregs using bias-extension test. J Thermoplast Compos Mater 2014;27:679–98. https://doi.org/10.1177/0892705712454289.
[31] Lebrun G, Bureau MN, Denault J. Evaluation of bias-extension and picture-frame test methods for the measurement of intraply shear properties of PP/glass commingled fabrics. Compos Struct 2003;61:341–52. https://doi.org/10.1016/S0263-8223(03)00057-6.
[32] Boisse P, Hamila N, Guzman-Maldonado E, Madeo A, Hivet G, dell'Isola F. The bias-extension test for the analysis of in-plane shear properties of textile composite reinforcements and prepregs: a review. Int J Mater Form 2017;10:473–92. https://doi.org/10.1007/s12289-016-1294-7.
[33] Khan MA, Pasco C, Reynolds N, Kendall K. Shear deformability characteristics of a rapid-cure woven prepreg fabric. Int J Mater Form 2020. https://doi.org/10.1007/s12289-019-01532-0.

[34] Pazmino J, Carvelli V, Lomov SV. Formability of a non-crimp 3D orthogonal weave E-glass composite reinforcement. Compos Part A Appl Sci Manuf 2014;61:76–83. https://doi.org/10.1016/j.compositesa.2014.02.004.

[35] Abdul Ghafour T, Colmars J, Boisse P. The importance of taking into account behavior irreversibilities when simulating the forming of textile composite reinforcements. Compos Part A Appl Sci Manuf 2019;127:105641. https://doi.org/10.1016/j.compositesa.2019.105641.

[36] Boisse P, Colmars J, Hamila N, Naouar N, Steer Q. Bending and wrinkling of composite fiber preforms and prepregs. A review and new developments in the draping simulations. Compos Part B Eng 2018;141:234–49. https://doi.org/10.1016/j.compositesb.2017.12.061.

[37] Creech G, Pickett AK. Meso-modelling of Non-Crimp Fabric composites for coupled drape and failure analysis. J Mater Sci 2006;41:6725–36. https://doi.org/10.1007/s10853-006-0213-6.

[38] Lim TC, Ramakrishna S, Shang HM. Strain field of deep drawn knitted fabric reinforced thermoplastic composite sheets. J Mater Process Technol 2000;97:95–9. https://doi.org/10.1016/S0924-0136(99)00336-2.

[39] Trejo EA. Characterizing the deformation response of a unidirectional non-crimp fabric for the development of computational draping simulation models, Master’s Thesis University of Waterloo, 2020. http://hdl.handle.net/10012/15974

[40] Härtel F, Harrison P. Evaluation of normalisation methods for uniaxial bias extension tests on engineering fabrics. Compos Part A Appl Sci Manuf 2014;67:61–9. https://doi.org/10.1016/j.compositesa.2014.08.011.

Journal Pre-proofs